Catalysis Science & Technology

ROYAL SOCIETY OF CHEMISTRY

PAPER

View Article Online
View Journal

Published on 11 October 2022. Downloaded by University of Oregon on 10/28/2022 1:40:49 AM.

Check for updates

Cite this: DOI: 10.1039/d2cy01280d

Tuning CO_2 hydrogenation selectivity on Ni/TiO_2 catalysts *via* sulfur addition†

Carole Le Berre,[a] Andrea Falqui,[b] Alberto Casu,[c] Tekalign T. Debela,[d] Mathias Barreau,[e] Christopher H. Hendon [d] and Philippe Serp [*a]

Received 19th July 2022,
Accepted 28th September 2022

DOI: 10.1039/d2cy01280d

rsc.li/catalysis

In the context of CO_2 valorization, the possibility of shifting the selectivity of Ni catalysts from CO_2 methanation to reverse water gas shift reaction could be economically attractive provided that the catalyst presents sufficient activity and stability. Remarkably, the addition of sulfur (0.2–0.8% w/w) to nickel on a Ni/TiO_2 catalyst induces a complete shift in the catalyst selectivity for CO_2 hydrogenation at 340 °C from 99.7% CH_4 to 99.7% CO. At an optimal Ni/S atomic ratio of 4.5, the productivity of the catalyst reaches 40.5 mol_{CO_2} mol_{Ni}^{-1} h^{-1} with a good stability. Density functional theory (DFT) calculations performed on various Ni surfaces reveal that the key descriptor of selectivity is the binding energy of the CO intermediate, which is related to the local electron density of surface Ni sites.

Introduction

Efficient CO_2 conversion using green H_2 coming from renewable sources represents a potential way to limit global CO_2 emission. Useful CO_2-derived C1 building blocks, such as formic acid, carbon monoxide, methanol and methane, can be obtained from the catalytic hydrogenation of CO_2. Among these C1 building blocks, CO, which can be used as a syngas component to be subsequently transformed into liquid fuels *via* Fischer–Tropsch synthesis (FTS), and CH_4, which represent a pillar of the power-to-gas technology,[1] are particularly attractive. On supported nickel catalysts, the reaction leads to methane formation (Sabatier reaction).[2,3] Noble metal-based catalysts are usually preferred for CO production *via* the reverse water gas shift reaction (RWGSR).[4] Considering the low cost of nickel compared to noble metals, shifting the selectivity of Ni catalysts from methanation to RWGSR could be economically attractive provided that the catalyst presents sufficient activity and stability.

It was recently reported that supported Ni single atoms[5–7] and, to a lesser extent, supported Ni clusters[8–12] could be active for the RWGSR, unravelling structure sensitivity in Ni-catalyzed CO_2 hydrogenation (decreasing CO adsorption strength with decreasing particle size). However, such catalysts present the drawback of being difficult to prepare at high metal loadings and on a large scale for industrial use. Another way to shift the selectivity of Ni towards CO is to modify its valence state such as in perovskites,[13,14] since the CO binding energy is much weaker on oxidized than on metallic-Ni.[15] At 400 °C, a $LaFe_{0.5}Ni_{0.5}O_3$ catalyst allows a STY of 8.7 mol_{CO} mol_{Ni}^{-1} h^{-1} with a S_{CO} of 96.6%.[13]

Tuning the selectivity of Ni catalysts was also achieved by controlling the nature of the metal-oxide interfacial sites,[16] which are suspected to be key species for the methanation of CO_2 and the RWGS reaction.[17–21] Experimental and theoretical results have demonstrated that on Ni_3Fe_3/ZrO_2 catalysts, the interaction of the Ni–ZrO_2 interface with CO was strong enough to facilitate CH_4 formation, while weak CO interaction on the Ni–FeO_x interface of Ni_3Fe_9/ZrO_2 catalysts made it desorb as the reaction product (at 400 °C, STY = 82.5 mol_{CO} mol_{Ni}^{-1} h^{-1} – S_{CO} = 95.8%).[16] Modifications in the Ni electronic structure can also be achieved by pretreating conventional Ni supported catalysts. For example, it has been demonstrated that the selectivity of Ni/SiO_2 catalysts was found to change from CH_4 to CO after a CO_2 hydrogenation cycle from 100 to 800 °C, due to the formation of Ni_3C presenting a lower CO adsorption energy than metallic Ni.[22] The formation of alloys[23] or intermetallic compounds[24] is also an efficient way to tune the metal d-band center, which proves to be instructive in assessing the binding energy of σ-donor intermediates, such as CO.

[a] *LCC-CNRS, INPT, 205 route de Narbonne, 31077 Toulouse Cedex 4, France. E-mail: philippe.serp@ensiacet.fr*
[b] *Department of Physics "Aldo Pontremoli", University of Milan, Via Celoria 16, 20133, Milan, Italy*
[c] *King Abdullah University of Science and Technology (KAUST), Biological and Environmental Sciences and Engineering (BESE) Division, 23955-6900 Thuwal, Saudi Arabia*
[d] *Department of Chemistry and Biochemistry, University of Oregon, Eugene, OR, USA*
[e] *ICPEES-UMR 7515 CNRS-ECPM-Université de Strasbourg, 25 rue Becquerel, 67087 Strasbourg Cedex 2, France*

† Electronic supplementary information (ESI) available: Catalytic performances, SEM, TEM, XRD, XPS, Raman, TPR and ESR analyses. See DOI: https://doi.org/10.1039/d2cy01280d

Published on 11 October 2022. Downloaded by University of Oregon on 10/28/2022 1:40:49 AM.

Sulfur has long been identified as a poison for Ni catalysts in CO-methanation, due to the quick and irreversible formation of inactive NiS sites that lead to the loss of catalytic activity due to geometric and electronic surface restructuring, terminally affecting the electronic properties of the Ni sites.[25–29] The activity loss is particularly significant in the case of pre-sulfided Ni catalysts.[25,29] For CO_2-methanation, on conventional supports such as alumina or silica, the presence of traces of sulfur impurities (H_2S, SO_2) in the feed gas,[30,31] or the use of a sulfate precursor during catalyst preparation[32] (the methanation being conducted without sulfur impurities), also results in a drastic activity decrease. Thus, a Ni/SiO_2 catalyst prepared from Ni sulfate showed negligible activities for CO_2 hydrogenation because of the formation of inactive Ni_3S_2 during catalyst preparation.[32] Interestingly, a higher tolerance of Ni catalysts to sulfur poisoning was evidenced when using a reducible support such as CeO_2, due to the thermodynamically favorable formation of the Ce_2O_2S phase that restricts the formation of nickel sulfide.[33] In addition, infrared studies on the effect of sulfur poisoning on the CO adsorption by Ni catalysts have shown that the strength of CO adsorption to surface nickel atoms was weaker on pre-sulfided catalysts.[34,35] Strong reduction or even blocking of CO adsorption upon sulfur addition to Ni(111) was also reported.[36] Finally, it is worth mentioning that (Fe, Ni)S clusters of natural enzymes, such as carbon monoxide dehydrogenase, efficiently and reversibly catalyze the reduction of CO_2 to CO.[37] Additionally, recent DFT calculations have shown the potentiality of the sulfur-deficient FeS(001) surface for CO_2 activation and reduction.[38] In that latter case, a high sulfur vacancy density is expected to improve the catalytic activity of FeS-containing catalysts for the RWGSR. However, to the best of our knowledge, there are no discussions in the literature about controlling the selectivity of CO_2 hydrogenation by sulfur addition on Ni catalysts.

Herein we demonstrate the effect of sulfidation on the selectivity of the Sabatier reaction on Ni/TiO_2 catalysts. Using a combination of first-principles calculations and experiments, we show that the selectivity of NiS_x/TiO_2 for the selective formation of CO over CH_4 can be tuned by controlling the extend of sulfidation (x). Our findings suggest that despite sulfur being a traditional poison for the Sabatier reaction on Ni, the incorporation of sulfidation offers one unique avenue to tune catalyst selectivity.

Results and discussion

Two Ni catalysts supported on the reducible oxide TiO_2 were first compared. The first one (10% Ni/TiO_2) was prepared by the incipient-wetness impregnation method from nickel nitrate using TiO_2-P25 as a support (a mixture of TiO_2 rutile (80%) and anatase (20%) phases).[18] The second one (10% Ni–S/TiO_2) was prepared similarly but the calcination was performed in the presence of SO_2, resulting after reduction in a sulfided catalyst. The catalytic performance using a flow reactor is shown in Fig. 1, and the results obtained after the reaction reached a steady-state at 260 and 340 °C are summarized in Table 1.

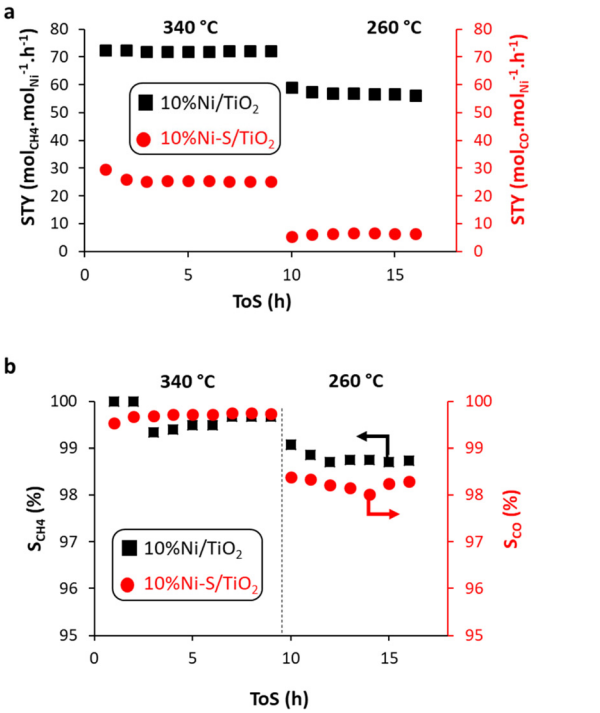

Fig. 1 Comparison of: a) STY in CO_2 methanation and b) CH_4/CO selectivity for $10Ni/TiO_2$ (black squares) and 10Ni–S/TiO_2 (red circles) catalysts at 340 and 260 °C. Reaction conditions: 200 mg catalyst, F/W = 16 500 mL g^{-1} h^{-1}, H_2/CO_2 = 4, P = 6.1 bar.

It is noticed that at temperatures as low as 260 °C, the 10% Ni/TiO_2 catalyst produces selectively CH_4 (S_{CH_4} = 98.7%) with a high activity (56.5 mol_{CH_4} mol_{Ni}^{-1} h^{-1}), while CO is selectively produced on 10% Ni–S/TiO_2 (S_{CO} = 98.3%) at a lower rate (6.5 mol_{CO} mol_{Ni}^{-1} h^{-1}).

As CH_4 selectivity can increase at high CO_2 conversion, we also run the 10% Ni/TiO_2 catalyst at lower conversion (Fig. S1†). Under these conditions (higher F/W ratio), the CO_2 conversion at 260 °C (4.3%) is similar to that obtained with Ni–S/TiO_2 (7.5%), and the Ni/TiO_2 catalyst is still very selective for CH_4 (S_{CH_4} > 94%). The temperature increase (up to 400 °C) significantly affects the CO_2 conversion, but not the selectivity (Fig. S2†). This sulfided catalyst shows interesting performances compared to other nickel catalysts active for the RWGSR reported in the literature (Table S1†). Indeed, a selectivity of 99.1% and a CO_2 conversion rate of 60.6 mol_{CO_2} mol_{Ni}^{-1} h^{-1} were obtained, which are similar to those obtained on a Ni/SiO_2 catalyst presenting a nickel carbide-like phase obtained after surface modification upon exposure to CO_2/H_2 or CH_4 atmospheres at high temperature.[22] The F/W ratio was further increased to 33 000 mL g^{-1} h^{-1} without impact on the selectivity (Fig. S3, Table S1†). As expected,[39] the CO_2 conversion decreased with the increase in F/W because of the shorter contact time and the

 This journal is © The Royal Society of Chemistry 2022

Published on 11 October 2022. Downloaded by University of Oregon on 10/28/2022 1:40:49 AM.

Table 1 CO_2 conversion, CH_4 and CO selectivity, and specific activity of Ni catalysts at 260 °C and 340 °C

Catalyst	CO_2 conv.[a] (%)	S_{CH_4}[a] (%)	S_{CO}[a] (%)	STY[b]
10Ni/TiO_2	79.1 (99.7)	98.7 (99.7)	1.3 (0.3)	56.5 (72.1)
10Ni–S/TiO_2	7.5 (29.2)	1.7 (0.3)	98.3 (99.7)	6.5 (25.2)

[a] The values between parentheses are the values obtained at 340 °C. [b] In $mol_{CH_4}\ mol_{Ni}^{-1}\ h^{-1}$ for 10Ni/TiO_2 and in $mol_{CO}\ mol_{Ni}^{-1}\ h^{-1}$ for 10Ni–S/TiO_2. Reaction conditions: 200 mg catalyst, F/W = 16 500 mL $g^{-1}\ h^{-1}$, H_2/CO_2 = 4, P = 6.1 bar.

decrease in the adsorbed reactant content on the catalyst surface.

It was checked that the operative pressure has no influence on the selectivity of the reaction (see Fig. S4† for the performance obtained at atmospheric pressure). A 1% Pt/TiO_2 catalyst (effective loading from ICP 1.02%) was also prepared for comparison purposes, since Pt based catalysts are conventional RWGS catalysts.[40] The comparison of the catalytic performance (Fig. S5†) shows that the 10% Ni–S/TiO_2 catalyst compared favorably at 340 °C, which is an excellent result considering the price of Pt metal. We nevertheless note that at 400 °C (Fig. S2†), the catalyst tends to slightly deactivate upon time on stream, and starts to form more CH_4, likely due to a partial reduction of some sulfide species, as discussed later.

ICP analyses show Ni contents of 9.1 and 7.6% w/w for 10% Ni/TiO_2 and 10% Ni–S/TiO_2 catalysts, respectively. Elemental analysis shows a S content of 0.32% w/w for the 10% Ni–S/TiO_2 catalyst (Table 2); this correspond to an atomic% of sulfur of 7.1% related to Ni. SEM observations performed on both catalysts (Fig. S6†) do not show remarkable morphological differences. Fig. 2 shows the STEM and STEM-HAADF images of the two freshly reduced catalysts. Particle size distributions based on total particle number and on total atom number[41] are shown in Fig. S7.† The average particle size for the 10% Ni/TiO_2 and 10% Ni–S/TiO_2 catalysts is 13.3 and 7.6 nm, respectively (Table 2). The smaller mean particle size obtained on the Ni–S/TiO_2 catalyst could be the result of a different metal–support interaction and an easier reduction for this catalyst, as discussed later. EDX analyses (Fig. S8†) were performed on the reduced catalysts to check for the presence of sulfur. Sulfur was not detectable on the 10Ni/TiO_2 catalyst, neither on the support nor on Ni. For the 10Ni–S/TiO_2 catalyst, sulfur was detected on the Ni particles (at% of S related to Ni between 2 and 15%), but was not detectable on the support.

Thus, if TiO_2–SO_4^- species could be formed upon catalyst calcination under SO_2/air mixtures,[42] these species should disappear upon catalyst reduction. To verify this hypothesis, we independently study by XRD the reaction of the $TiOSO_4 \cdot xH_2O$ reference compound under the conditions used for catalyst reduction. The data obtained (Fig. S9†) point to the complete transformation of $TiOSO_4 \cdot xH_2O$ into anatase TiO_2 under these reducing conditions.

HRSTEM-HAADF analysis of the 10% Ni–S/TiO_2 catalyst provided better-defined information from a spatial point of view and highlighted the rare presence of small-sized nanoparticles at the edges of wider crystalline domains. While the structures of the latter are compatible with TiO_2, local Fourier analysis performed on these small nanoparticles (<5 nm) showed a sufficiently clear structural projection resulted in finding different sets of interplanar distances and angular relationships that could be ascribed to distinct phases of nickel sulfide, namely NiS, NiS_2 and Ni_3S_2 (Fig. 3). To understand the structural transformation of the catalyst during the sulfidation, XRD analyses were performed (Fig. S10†). The Ni diffraction peaks of the 10Ni/TiO_2 catalyst (2θ = 44.5°, 51.9°, and 76.3°) correspond to the (111), (200), and (220) crystal faces of Ni. For the 10Ni–S/TiO_2 catalyst, these peaks are much wider and less intense, but still present (2θ = 44.3°, 51.9°, and 76.3°). Given the low occurrence and the small size of many of the crystalline nickel sulfide nanoparticles observed by HRSTEM-HAADF analysis, the presence of a crystalline sulfided phase (NiS, NiS_2 or Ni_2S_3) could not be clearly detected by XRD, but the wide peaks observed could also fit some peaks of Ni sulfide phases. Finally, the presence of amorphous nickel sulfide nanoparticles cannot be ruled out from STEM and XRD analyses.

The Ni crystallite size measured by XRD was 16.5 and 9.2 nm for the 10% Ni/TiO_2 and 10% Ni–S/TiO_2 catalysts, respectively, which is in good accordance with the STEM-HAADF measurements. XPS analyses were performed just after reducing the samples at 400 °C. Fig. S11† presents the high-resolution Ni 2p, S 2p and Ti 2p spectra of the two samples. The Ni 2p spectra are composed of two spin–orbit doublets ($2p_{1/2}$ and $2p_{3/2}$) and shakeup satellites. For the 10% Ni/TiO_2 catalyst (Fig. 4a), Ni is present as Ni^0 (main peak at

Table 2 Catalyst characterization

Catalyst	Ni (%)	S (%)	BET surface area ($m^2\ g^{-1}$)	Ni particle size[a] (nm)	Ni particle size[b] (nm)
10% Ni/TiO_2	9.1	0	42.9	16.5	13.3 ± 1.8
10% Ni–S/TiO_2	7.6	0.32	49.1	9.2	7.6 ± 1.5

[a] From XRD. [b] From TEM.

Published on 11 October 2022. Downloaded by University of Oregon on 10/28/2022 1:40:49 AM.

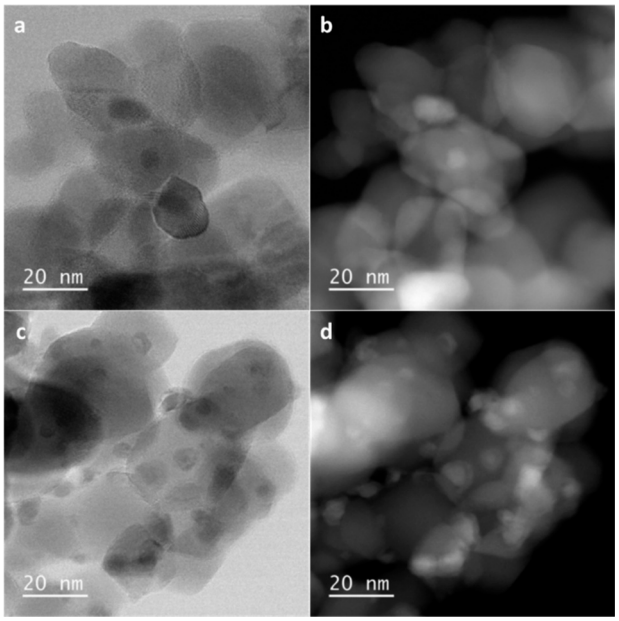

Fig. 2 STEM and STEM-HAADF micrographs of the reduced: a and b 10% Ni/TiO_2; and c and d 10% $Ni–S/TiO_2$ catalysts.

852.6 eV),[43] NiO (multiplet-split peaks at 853.7 and 855.8 eV)[44] and possibly $Ni(OH)_2$ (855.8 eV).[45,46] The presence of a significant amount of Ni^0 can explain the high selectivity for methane obtained with this catalyst. The Ni $2p_{3/2}$ core-level spectrum of the 10% $Ni–S/TiO_2$ catalyst is significantly different (Fig. 4b), showing a very small contribution of Ni^0 (852.6 eV) and an intense peak at 856.3 eV, which could arise from $Ni(OH)_2$, NiS (855.7 eV),[47] Ni_3S_2 (855.7–856.1 eV)[48,49]

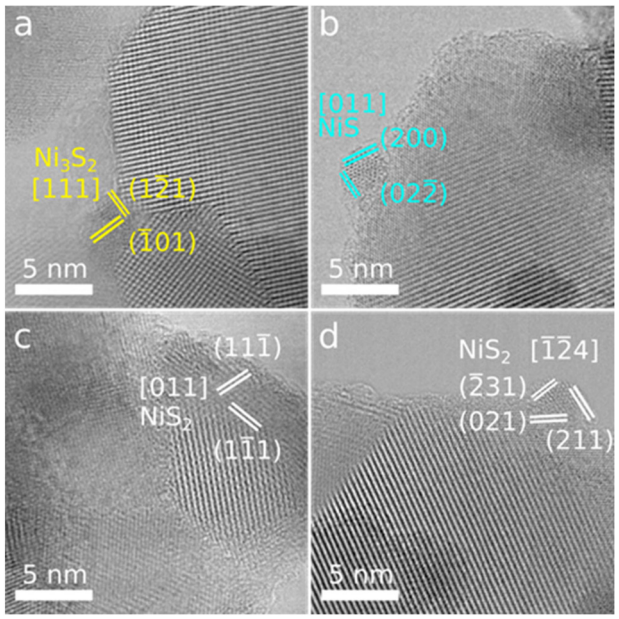

Fig. 3 Representative HRSTEM-HAADF micrographs of the 10% Ni–S/TiO_2 catalyst, showing small crystal domains of different nickel sulfide phases with interplanar distances indicated in false colors: a) Ni_3S_2 (yellow), b) NiS (cyan), c and d) NiS_2 (white).

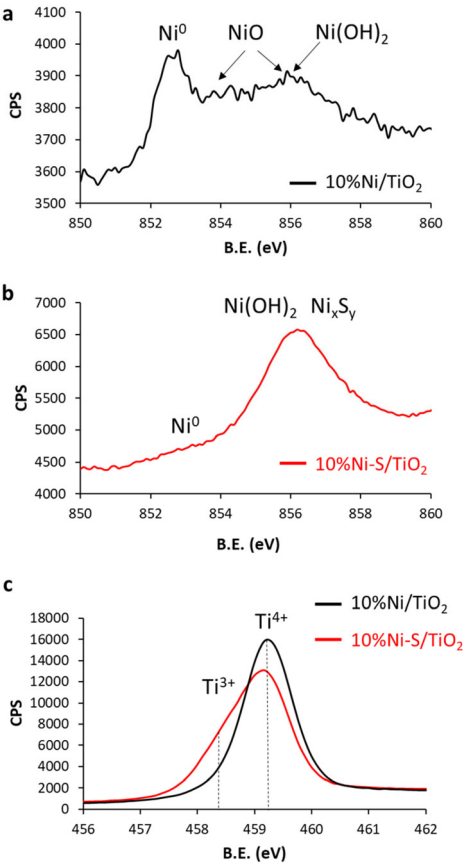

Fig. 4 Ni 2p XPS spectra of 10% Ni/TiO_2 (a) and 10% $Ni–S/TiO_2$ (b); and (c) Ti 2p XPS spectrum of $Ni–S/TiO_2$ and Ni/TiO_2.

and/or NiS_2 (855.7–855.9 eV).[50,51] The Ni/S surface atomic ratios of the 10% $Ni–S/TiO_2$ catalyst allow the calculation of an atomic% of S related to Ni of 7.6% (in good accordance with the values obtained from elemental and EDX analyses) that precludes the exclusive formation of NiS. For the S 2p spectrum, the peak at 162.1 eV corresponds to divalent ions (S^{2-}) involved in metal–sulfur bonds,[52] which could correspond to NiS (161.6 eV), Ni_3S_2 (162.2 eV) and/or NiS_2 (162.4 eV).[51,53] The peak at 168.9 eV is associated with sulfate species resulting from surface oxidation of NiS_x species.[51,54] The high-resolution Ti $2p_{3/2}$ XPS spectra of the 10% Ni/TiO_2 and 10% $Ni–S/TiO_2$ catalysts are shown in Fig. 4c. For 10% Ni/TiO_2, the Ti $2p_{3/2}$ and Ti $2p_{1/2}$ peaks centered at binding energies of 459.3 and 465.2 eV (Fig. S10†) are typical of the Ti^{4+}–O bonds in TiO_2. In 10% $Ni–S/TiO_2$, the envelop of the Ti $2p_{3/2}$ peak is broader due to the presence of Ti^{3+} species at 458.3 eV, resulting from the creation of surface oxygen vacancies (O_v).[47] The attribution of the 458.3 eV component to titanium(IV) oxysulfate species must be excluded on the basis of XPS measurements over the $TiOSO_4{\cdot}xH_2O$ reference compound (Fig. S12†). The formation of O_v upon sulfidation/reduction was confirmed by Raman analyses (Fig. S13†). The lowest frequency vibrational mode $E_g(1)$ at 140 cm^{-1} characteristic of TiO_2 in 10% Ni/TiO_2 shows pronounced broadening and blue-shift (149 cm^{-1}) in 10% $Ni–S/TiO_2$.

This journal is © The Royal Society of Chemistry 2022

Published on 11 October 2022. Downloaded by University of Oregon on 10/28/2022 1:40:49 AM.

Theoretical calculations proposed that the broadening and blue-shift resulted from the presence of localized lattice defects associated with surface O_v.[55] The formation of O_v on TiO_2 leads to the creation of unpaired electrons or cationic Ti^{3+} centers observable by EPR.[56,57]

The EPR spectrum of 10% Ni–S/TiO_2 (Fig. S14†) shows a broad EPR resonance line at g = 2.156, which could arise from surface exposed Ti^{3+} sites but also from Ni^{3+} species.[58,59] The presence of a significant amount of O_v on the 10% Ni–S/TiO_2 catalyst can be of importance for the CO_2 hydrogenation reaction. Indeed, it has been proposed that on Ni/TiO_2 catalysts, the presence of Ti^{3+}species, which likely altered the SMSI between Ni and the support, allows the enhancement of CO_2 hydrogenation activity.[60] It is also known that $Ni^{\delta-}$–O_v–Ti^{3+} interfacial sites on Ni/TiO_2 catalysts serve as dual-active sites to efficiently catalyse the WGSR.[61–63]

The TPR profiles of the supported nickel catalysts are shown in Fig. S15.† They indicate a different metal–support interaction in the two catalysts. The reduction temperature maxima (RTM) peaks were located at 510 °C for 10% Ni/TiO_2 and 460 °C for 10% Ni–S/TiO_2. Similar differences in RTM have been reported for Ni/Al_2O_3 and $NiSO_4$/Al_2O_3 catalysts.[64] Also, the shape of the TPR curve for the 10% Ni–S/TiO_2 catalyst is less symmetrical, which indicates a less uniform state of the nickel species in this catalyst. The reduction peak of the 10% Ni–S/TiO_2 catalyst begins at 360 °C, which may explain the slight catalyst deactivation observed when the RWGSR is carried out at 400 °C (Fig. S2†).

Together, the 10% Ni/TiO_2 catalyst presents several features of a good methanation catalyst: relatively large particle size and predominance of $Ni^{(0)}$.[18] The 10% Ni–S/TiO_2 catalyst contains significant amounts of O_v on the support, which are active for CO_2 activation.[12] This catalyst contains few $Ni^{(0)}$ for H_2 activation (H_2 heterolytic dissociation can also occur on sulfided catalysts[65]), and significant amounts of amorphous and crystalline NiS_x species. As it has been shown that the strength of CO adsorption to surface Ni atoms was weaker for pre-sulfided catalysts,[34,35] we can propose that this is the origin of the high selectivity for the RWGSR observed for the Ni–S/TiO_2 catalyst.

In order to understand the correlation between the binding energy of CO and the product selectivity, we calculated the CO adsorption energies (E_a) for Ni(111), Ni_3S_2(001), NiS(100) and NiS_2(111) surfaces using the spin-polarized DFT. We sampled several plausible CO binding modes to various facets of the Ni_xS_y systems (Fig. S16 and Table S2†), and show the most stable CO-bound configurations in Fig. 5. We find the binding energies to be −1.57, −1.47, −0.73, and −1.20 eV for Ni(111), Ni_3S_2(001), NiS(100), and NiS_2(111) surfaces, respectively. The results indicate that the Ni(111) surface binds CO most strongly. The addition of sulfur leads to weakening of the CO binding. The CO binding energy is inversely proportional to the degree of sulfidation. We can understand this through examination of the Ni d-band center. Since CO is both a σ-donor and π-acceptor, the CO bond energy should be reduced as the

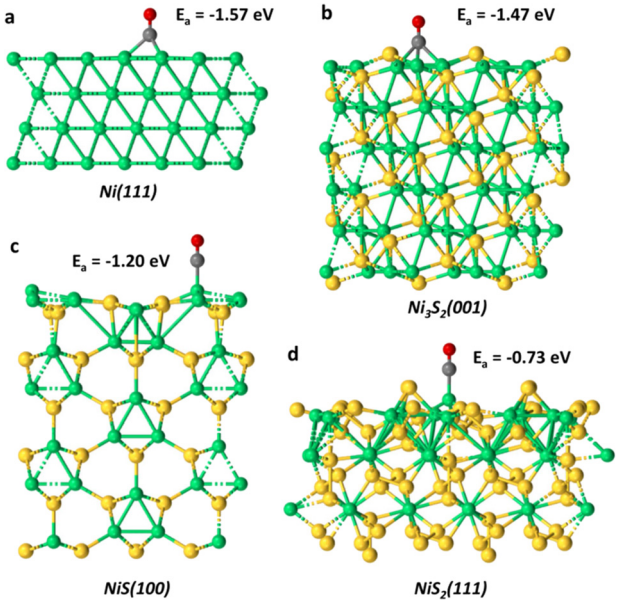

Fig. 5 DFT equilibrated structure of CO chemisorbed on a) Ni(111), b) Ni_3S_2(001), c) NiS(100), and d) NiS_2(111) surfaces.

metal d-states are occupied, as the d-center is a descriptor for σ-accepting ability. Thus, a downward shift of the d-band center is considered favorable because it correlates with the decrease in adsorption energies of typical catalytic σ-donor and π-acceptor poisons, such as CO, resulting in the turnover of surface active sites.[66]

In our case, the calculated Ni d-band centers are −0.30, −1.14, −1.34, and −1.37 eV for Ni(111), Ni_3S_2(001), NiS(100), and NiS_2(111) surfaces, respectively. This trend supports the hypothesis that sulfidation is one route to affecting CO-binding energies, thereby affecting the catalytic preference to form CO over CH_4. We also considered possible CO_2 binding sites on the Ni_xS_y systems (Fig. S17†), but did not include the energetics of these species in this study. Instead, we focus on the CO binding energy as an energetic descriptor for selectivity.

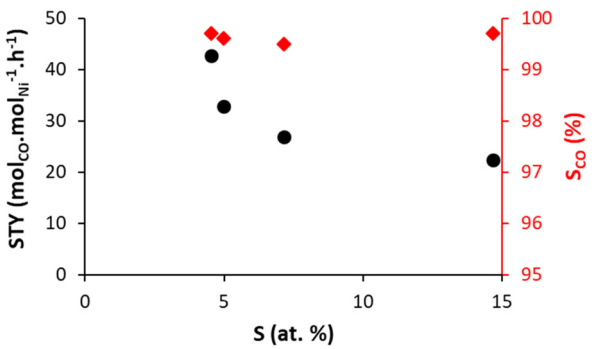

Fig. 6 Comparison of: STY (black circles) and CO selectivity (red diamonds) for 10Ni–S/TiO_2 catalysts presenting various sulfur% related to Ni. Reaction conditions: T = 340 °C, 200 mg catalyst, F/W = 16 500 mL g^{-1} h^{-1}, H_2/CO_2 = 4, P = 6.1 bar.

Published on 11 October 2022. Downloaded by University of Oregon on 10/28/2022 1:40:49 AM.

Finally, as the Ni/S atomic ratio could have an influence on both activity and selectivity, we used different pre-sulfided catalysts showing sulfur atomic percentage related to nickel between 4.5 and 15% (based on elemental and ICP analyses) to evaluate its impact. Fig. 6 shows the catalytic performances of these catalysts for the RWGSR performed at 340 °C. In the investigated range, the atomic% of sulfur related to Ni significantly affects the catalyst activity, with an optimum value at 4.5%, but has no influence on selectivity.

Conclusions

In summary, we have demonstrated a facile strategy to tune the selectivity of a Ni/TiO_2 catalyst in the CO_2 hydrogenation reaction. Calcination of the Ni/TiO_2 catalyst under SO_2–air mixtures allows after reduction a sulfided Ni–S/TiO_2 catalyst to be obtained. The sulfided catalyst contains significant amounts of O_v to activate CO_2, metallic nickel or sulfided Ni (ref. 67) for H_2 activation and significant amounts of amorphous and crystalline NiS_x species. Compared to the Ni/TiO_2 catalyst that produces selectively CH_4 in the 260–400 °C temperature range, the Ni–S/TiO_2 catalyst is less active but selectively produces CO in the same temperature range, while maintaining a good stability below 340 °C. According to DFT calculations, the key descriptor of selectivity is the CO binding energy to the Ni surface, which is related to the position of the d-band centre of the Ni species. Notably, while sulfur has long been identified as a poison for Ni catalysts in CO-methanation, we have demonstrated that its association with Ni on a reducible support such as TiO_2 allows the production of a precious metal-free RWGSR catalyst.

Experimental section

Catalyst preparation

The Ni catalysts were prepared by using an impregnation method. $Ni(NO_3)_2{\cdot}6H_2O$ (99.9% Strem Chemical) was dissolved in water, where $TiO_{2\text{-}P25}$ (99.5%, Aeroxide, Aldrich) was then added. The desired quantity of $Ni(NO_3)_2{\cdot}6H_2O$ to reach a 10% w/w was used. The mixture was stirred for 4 h. The water was evaporated to obtain the catalyst, which was dried at 120 °C overnight, and calcined at 500 °C for 6 h under air to produce the calcined 10% Ni/TiO_2 catalyst. A similar procedure was followed to prepare the 10% Ni–S/TiO_2 catalyst, but in that case the calcination was performed in the presence of SO_2–air mixtures obtained by mixing SO_2 with air, with the SO_2 concentration in the gas–air mixture being in the range of 0.2–5 g m^{-3}. The amount of nickel deposited on each support was determined by inductively coupled plasma (ICP) analyses.

A 1% Pt/TiO_2 catalyst was also prepared for comparative purposes by using the impregnation method from tetraammineplatinum(II) nitrate.

Catalyst characterization

The structural and textural properties of the catalysts were evaluated using different characterization techniques. The Brunauer–Emmett–Teller (BET) surface area, pore volume and pore size distribution of the samples were measured using a Quantachrome Autosorb instrument with N_2 automatic injection. This method permits the N_2 adsorption/desorption isotherms to be obtained at −196 °C. All the samples were pretreated under vacuum at 90 °C for 1 h to remove adsorbed water, then at 250 °C for 10 h for all other physisorbed species.

For the Temperature-Programmed Reduction (TPR) experiment (Micromeritics AutoChem 2920 Analyzer), the catalyst (100 mg) was introduced in a U-shaped tube and placed in an oven. Firstly, it was heated to 200 °C (10 °C min^{-1}) for 1 h. After the reactor cooled to room temperature, an argon flow (30 mL min^{-1}) swept the sample for 30 minutes. In the second step, the catalyst was reduced under a gaseous mixture of 10% H_2/Ar (30 mL min^{-1}) with a heating ramp of 10 °C min^{-1} to 850 ° C. The amount of hydrogen consumed was monitored using a TCD. The peaks of hydrogen consumption were obtained as a function of the temperature.

The distribution, shape and size of the metal particles were obtained using a JEOL JEM 1011 transmission electron microscope (TEM). High-resolution analyses were conducted by using a JEOL JEM 2100F equipped with a field emission gun (FEG) operating at 200 kV with a point resolution of 2.3 Å and a JEOL JEM-ARM200F Cold FEG operating at 200 kV with a point resolution of >1.9 Å.

The crystalline structure of the samples was determined using a D8 Advance Bruker diffractometer (XRD). The surface of a sample to a depth of 1 to 10 nm was observed by X-ray Photoelectron Spectroscopy (XPS) using a Thermo Scientific K-alpha spectrometer equipped with an aluminum monochromatic source (Al Kα, $h\nu$ = 1486.6 eV). Raman measurements were recorded with a Raman Horiba Jobin Yvon Labram HR 800 spectrometer in backscattering geometry using an optical objective 100 (NA 0.9). The wavelength of the incident laser was 532 nm and its power was set to 1 mW. EPR data were recorded using an Elexsys E 500 Bruker spectrometer, operating at a microwave frequency of ≈9.5 GHz. All spectra were recorded using a microwave power of 10 mW across a sweep width of 1500 G (centred at 3100 G) with a modulation amplitude of 2 G. Experiments were carried out at 10 K using a liquid helium cryostat.

Catalytic tests

The catalytic tests of CO_2 hydrogenation were performed using a continuous-flow stainless steel fixed bed reactor (height = 300 mm, e.d. = 9.52 mm, i.d. = 7.9 mm) under a total pressure of 6.1 bar. 200 mg of catalyst with a particle size in the 100–200 μm range were mixed with 1800 mg of SiC (Alfa Aesar). Before the catalytic test, the catalyst was reduced *in situ* at 400 °C for 4 h under a 1/4 mixture of N_2/

This journal is © The Royal Society of Chemistry 2022

Published on 11 October 2022. Downloaded by University of Oregon on 10/28/2022 1:40:49 AM.

H_2, at atmospheric pressure. Then, experiments were performed at a constant F/W ratio (molar flow of reactant per mass of catalyst) of 16 500 mL (g h)$^{-1}$. Catalytic tests were performed under a $N_2/H_2/CO_2$ gas mixture of 1/4/1 at 260, 300 and 340 °C and 6.1 bar. The composition of the reactant/product mixture was analyzed using an on-line gas chromatograph (500 Clarius) equipped with two TCDs: one with argon as the gas vector to quantify H_2, CH_4, and CO, and another with helium to quantify CO_2. The GC is equipped with two Shincarbon columns (1/8, 2.0 mm, 80/100), and recorded the formation of methane and conversion of H_2 and CO_2 every 8 min.

The different response coefficients determined from the GC calibration allowed us to calculate the molar fractions (X) of the different molecules considered during the methanation reaction, as follows:

$$X_A = \left(\frac{\text{Area of A signal}}{\text{Area of } N_2 \text{ signal}} \times N_2 \text{ flow}\right) \times \frac{1}{k_A}$$

With a = CO_2, CH_4, H_2, CO and k = response coefficient. The conversion rates of the reagents were then calculated as follows:

$$CO_2 \text{ conversion } (\%) = \left(1 - \frac{X_{CO_2}}{X_{CO_2} + X_{CH_4} + X_{CO}}\right) \times 100\%$$

$$H_2 \text{ conversion } (\%) = \left(1 - \frac{H_2 \text{ Output flow}}{H_2 \text{ Input flow}}\right) \times 100\%$$

With H_2 output flow = dry flow output x X_{H_2}.

$$\text{Dry flow output} = \left(\frac{CO_2 \text{ input flow}}{X_{CO_2} + X_{CH_4} + X_{CO}}\right)$$

$$CH_4 \text{ yield } (\%) = \left(\frac{CH_4 \text{ output flow}}{CO_2 \text{ input flow}}\right) \times 100\%$$

CH_4 output flow = dry flow output x X_{CH_4}.

$$CO \text{ yield } (\%) = \%\ CO_2 \text{ conversion} - CH_4 \text{ yield } (\%)$$

$$CH_4 \text{ selectivity } (\%) = \left(\frac{CH_4 \text{ yield } (\%)}{\%CO_2 \text{ conversion}}\right) \times 100\%$$

$$CO \text{ selectivity } (\%) = \left(\frac{CO \text{ yield } (\%)}{\%CO_2 \text{ conversion}}\right) \times 100\%$$

We expressed the percentage of CO_2 consumed by unit of time and by mole of metal, which corresponds to the STY.

Computational details

First-principles calculations were performed using spin-polarized DFT as implemented in the Vienna *ab initio* simulation package (VASP), version 5.4.4.[68,69] The projected augmented plane wave (PAW)[70,71] approach with a plane-wave kinetic energy cutoff of 500 eV, and the revised Perdew–Burke–Ernzerhof (RPBE)[72] exchange–correlation functional were employed. The Methfessel–Paxton method with broadening of 0.1 eV is used for the slabs, while Gaussian-smearing with 0.01 eV was used for the CO molecule.

Ni(111), Ni_3S_2(001), NiS(100),and NiS_2(111) surfaces were used to model the slab geometry. A vacuum space of 20 Å was used along the c-direction (perpendicular to the slabs) to ensure no significant interaction between adjacent cells occurred. For each surface, several competing binding modes were examined, and the most stable was presented. The others are available in the ESI.† Structural optimization was performed until the average force was <0.03 eV Å^{-1} and the total energy converged within 10^{-5} eV per atom. A Monkhorst–Pack K-point sampling of 3 × 3 × 1 was used for the slab geometry, while only the Γ-point was used for the free CO molecule. The adsorption energy is defined as $E_a = E_{tot} - E_{pristine} - E_{mol}$, where E_{tot}, $E_{pristine}$, and E_{mol} are the calculated energy of the slab with adsorbate, the pristine slab, and the CO molecule in the gas phase, respectively.

The d-band center was computed by aligning the mean d-states from the density of states to the Fermi level, following the method presented elsewhere.[66]

Author contributions

Dr. Carole Le Berre: catalyst synthesis and characterization and catalytic experiments, data elaboration and interpretation, writing original draft; Dr. Andrea Falqui and Dr. Alberto Casu: electron microscopy studies, data elaboration and interpretation; Prof. Christopher H. Hendon and Dr. Tekalign Debela: modeling studies, data elaboration and interpretation; Dr. Mathias Barreau: XPS studies; Prof. Philippe Serp: conceptualization and supervision of all the activities. All the authors contributed to the result discussion and review & editing of the manuscript.

Conflicts of interest

The authors do not have any conflict of interests to be declared.

Acknowledgements

This work was financially supported by "Région Occitanie" through a Readynov contract "Valorisation du CO_2 par méthanation catalytique" (2005314). Thanks to Marion Technologies for the scale-up of catalysts synthesized. TD and CHH are supported by the National Science Foundation through the Division of Materials Research under grant no. DMR-1956403 and the Camille and Henry Dreyfus Foundation. Computations were performed in the Extreme Science and Engineering Discovery Environment (XSEDE), which is supported by the National Science Foundation [ACI-1548562] and the PICS Coeus High Performance Computer,

Published on 11 October 2022. Downloaded by University of Oregon on 10/28/2022 1:40:49 AM.

which is supported by the National Science Foundation [1624776]. The authors acknowledge Dr. Spiros Zafeiratos (ICPEES-UMR 7515 CNRS-ECPM-Strasbourg University, France) for access to XPS.

Notes and references

1 M. Thema, F. Bauer and M. Sterner, *Renewable Sustainable Energy Rev.*, 2019, **112**, 775–787.
2 M. A. A. Aziz, A. A. Jalil, S. Triwahyono and A. Ahmad, *Green Chem.*, 2015, **17**, 2647–2663.
3 L. Li, W. Zeng, M. Song, X. Wu, G. Li and C. Hu, *Catalysts*, 2022, **12**, 244.
4 Y. A. Daza and J. N. Kuhn, *RSC Adv.*, 2016, **6**, 49675–49691.
5 M.-M. Millet, G. Algara-Siller, S. Wrabetz, A. Mazheika, F. Girgsdies, D. Teschner, F. Seitz, A. Tarasov, S. V. Levchenko, R. Schlögl and E. Frei, *J. Am. Chem. Soc.*, 2019, **141**, 2451–2461.
6 H. Shen, Y. Dong, S. Yang, Y. He, Q. Wang, Y. Cao, W. Wang, T. Wang, Q. Zhang and H. Zhang, *Nano Res.*, 2022, **15**, 5831–5841.
7 L. Wang, H. Liu, Y. Liu, Y. Chen and S. Yang, *J. Rare Earths*, 2013, **31**, 969–974.
8 C. Vogt, E. Groeneveld, G. Kamsma, M. Nachtegaal, L. Lu, C. J. Kiely, P. H. Berben, F. Meirer and B. M. Weckhuysen, *Nat. Catal.*, 2018, **1**, 127–134.
9 K. Feng, J. Tian, M. Guo, Y. Wang, S. Wang, Z. Wu, J. Zhang, L. He and B. Yan, *Appl. Catal., B*, 2021, **292**, 120191.
10 L. R. Winter, E. Gomez, B. Yan, S. Yao and J. G. Chen, *Appl. Catal., B*, 2018, **224**, 442–450.
11 H. C. Wu, Y. C. Chang, J. H. Wu, J. H. Lin, I. K. Lin and C. S. Chen, *Catal. Sci. Technol.*, 2015, **5**, 4154–4163.
12 C. Rivera-Cárcamo, C. Scarfiello, A. B. García, Y. Tison, H. Martinez, W. Baaziz, O. Ersen, C. Le Berre and P. Serp, *Adv. Mater. Interfaces*, 2021, **8**, 2001777.
13 B. Zhao, B. Yan, Z. Jiang, S. Yao, Z. Liu, Q. Wu, R. Ran, S. D. Senanayake, D. Weng and J. G. Chen, *Chem. Commun.*, 2018, **54**, 7354–7357.
14 H. S. Lim, M. Lee, Y. Kim, D. Kang and J. W. Lee, *Int. J. Hydrogen Energy*, 2021, **46**, 15497–15506.
15 Y. Wang, L. R. Winter, J. G. Chen and B. Yan, *Green Chem.*, 2021, **23**, 249–267.
16 B. Yan, B. Zhao, S. Kattel, Q. Wu, S. Yao, D. Su and J. G. Chen, *J. Catal.*, 2019, **374**, 60–71.
17 N. Rui, X. Zhang, F. Zhang, Z. Liu, X. Cao, Z. Xie, R. Zou, S. D. Senanayake, Y. Yang, J. A. Rodriguez and C.-J. Liu, *Appl. Catal., B*, 2021, **282**, 119581.
18 D. Messou, V. Bernardin, F. Meunier, M. B. Ordoño, A. Urakawa, B. F. Machado, V. Collière, R. Philippe, P. Serp and C. Le Berre, *J. Catal.*, 2021, **398**, 14–28.
19 S. Tada, H. Nagase, N. Fujiwara and R. Kikuchi, *Energy Fuels*, 2021, **35**, 5241–5251.
20 M.-X. Huang, F. Liu, C.-C. He, S.-Q. Yang, W.-Y. Chen, L. Ouyang and Y.-J. Zhao, *Chem. Phys. Lett.*, 2021, **768**, 138396.
21 G. Varvoutis, M. Lykaki, S. Stefa, V. Binas, G. E. Marnellos and M. Konsolakis, *Appl. Catal., B*, 2021, **297**, 120401.
22 T. S. Galhardo, A. H. Braga, B. H. Arpini, J. Szanyi, R. V. Gonçalves, B. F. Zornio, C. R. Miranda and L. M. Rossi, *J. Am. Chem. Soc.*, 2021, **143**, 4268–4280.
23 S. Lin, Q. Wang, M. Li, Z. Hao, Y. Pan, X. Han, X. Chang, S. Huang, Z. Li and X. Ma, *ACS Catal.*, 2022, **12**, 3346–3356.
24 J. Guo, Z. Wang, J. Li and Z. Wang, *ACS Catal.*, 2022, **12**, 4026–4036.
25 J. R. Rostrup-Nielsen and K. Pedersen, *J. Catal.*, 1979, **59**, 395–404.
26 C. H. Bartholomew, G. D. Weatherbee and G. A. Jarvi, *J. Catal.*, 1979, **60**, 257–269.
27 E. J. Erekson and C. H. Bartholomrw, *Appl. Catal.*, 1983, **5**, 323–336.
28 C. H. Bartholomew, in *Studies in Surface Science and Catalysis*, ed. B. Delmon and G. F. Froment, Elsevier, 1987, vol. 34, pp. 81–104.
29 B. Legras, V. V. Ordomsky, C. Dujardin, M. Virginie and A. Y. Khodakov, *ACS Catal.*, 2014, **4**, 2785–2791.
30 M. Wolf, C. Schüler and O. Hinrichsen, *J. CO2 Util.*, 2019, **32**, 80–91.
31 K. Müller, M. Fleige, F. Rachow and D. Schmeißer, *Energy Procedia*, 2013, **40**, 240–248.
32 X. Wen, L. Xu, M. Chen, Y. Shi, C. Lv, Y. Cui, X. Wu, G. Cheng, C.-E. Wu, Z. Miao, F. Wang and X. Hu, *Appl. Catal., B*, 2021, **297**, 120486.
33 A. Alarcón, J. Guilera, R. Soto and T. Andreu, *Appl. Catal., B*, 2020, **263**, 118346.
34 C. H. Rochester and R. J. Terrell, *J. Chem. Soc., Faraday Trans. 1*, 1977, **73**, 609–621.
35 M. Trenary, K. J. Uram and J. T. Yates, *Surf. Sci.*, 1985, **157**, 512–538.
36 W. Erley and H. Wagner, *J. Catal.*, 1978, **53**, 287–294.
37 J. Heo, C. R. Staples and P. W. Ludden, *Biochemistry*, 2001, **40**, 7604–7611.
38 N. Y. Dzade and N. H. de Leeuw, *Catalysts*, 2021, **11**, 127.
39 M. M. Jaffar, M. A. Nahil and P. T. Williams, *Energy Technol.*, 2019, **7**, 1900795.
40 M. Zhu, Q. Ge and X. Zhu, *Trans. Tianjin Univ.*, 2020, **26**, 172–187.
41 C.-T. Kuo, Y. Lu, L. Kovarik, M. Engelhard and A. M. Karim, *ACS Catal.*, 2019, **9**, 11030–11041.
42 B. Wang, X. Li, S. Liang, R. Chu, D. Zhang, H. Chen, M. Wang, S. Zhou, W. Chen, X. Cao and W. Feng, *Phys. Chem. Chem. Phys.*, 2020, **22**, 9943–9953.
43 W. Lin, H. Cheng, L. He, Y. Yu and F. Zhao, *J. Catal.*, 2013, **303**, 110–116.
44 A. N. Mansour, *Surf. Sci. Spectra*, 1994, **3**, 231–238.
45 A. N. Mansour and C. A. Melendres, *Surf. Sci. Spectra*, 1994, **3**, 255–262.
46 J. Yu, Y. Hai and B. Cheng, *J. Phys. Chem. C*, 2011, **115**, 4953–4958.
47 X. Zhang, Y. Chen, Y. Xiao, W. Zhou, G. Tian and H. Fu, *Nanoscale*, 2018, **10**, 4041–4050.
48 L. Hou, Q. Bu, S. Li, D. Wang and T. Xie, *RSC Adv.*, 2016, **6**, 99081–99087.

 This journal is © The Royal Society of Chemistry 2022

Published on 11 October 2022. Downloaded by University of Oregon on 10/28/2022 1:40:49 AM.

49 J. Wang, Z. Yang, J. Mei, C. Wang, Q. Hong and S. Yang, *J. Colloid Interface Sci.*, 2022, **622**, 431–442.
50 L. Zhang, I. S. Amiinu, X. Ren, Z. Liu, G. Du, A. M. Asiri, B. Zheng and X. Sun, *Inorg. Chem.*, 2017, **56**, 13651–13654.
51 H. Liu, Z. Liu, F. Wang and L. Feng, *Chem. Eng. J.*, 2020, **397**, 125507.
52 T.-F. Hung, Z.-W. Yin, S. B. Betzler, W. Zheng, J. Yang and H. Zheng, *Chem. Eng. J.*, 2019, **367**, 115–122.
53 Y. Nan, X. Wang, X. Ning, J. Lei, S. Guo, Y. Huang and J. Duan, *Surf. Coat. Technol.*, 2019, **377**, 124935.
54 G. B. Shombe, M. D. Khan, C. Zequine, C. Zhao, R. K. Gupta and N. Revaprasadu, *Sci. Rep.*, 2020, **10**, 3260.
55 A. Naldoni, M. Allieta, S. Santangelo, M. Marelli, F. Fabbri, S. Cappelli, C. L. Bianchi, R. Psaro and V. Dal Santo, *J. Am. Chem. Soc.*, 2012, **134**, 7600–7603.
56 J. Strunk, W. C. Vining and A. T. Bell, *J. Phys. Chem. C*, 2010, **114**, 16937–16945.
57 X. Pan, M.-Q. Yang, X. Fu, N. Zhang and Y.-J. Xu, *Nanoscale*, 2013, **5**, 3601–3614.
58 S.-H. Chien, Y.-W. Wei and M.-C. Lin, *J. Chin. Chem. Soc.*, 1997, **44**, 195–201.
59 S. Mohajernia, P. Andryskova, G. Zoppellaro, S. Hejazi, S. Kment, R. Zboril, J. Schmidt and P. Schmuki, *J. Mater. Chem. A*, 2020, **8**, 1432–1442.
60 J. Li, Y. Lin, X. Pan, D. Miao, D. Ding, Y. Cui, J. Dong and X. Bao, *ACS Catal.*, 2019, **9**, 6342–6348.
61 M. Xu, S. He, H. Chen, G. Cui, L. Zheng, B. Wang and M. Wei, *ACS Catal.*, 2017, **7**, 7600–7609.
62 M. Xu, S. Yao, D. Rao, Y. Niu, N. Liu, M. Peng, P. Zhai, Y. Man, L. Zheng, B. Wang, B. Zhang, D. Ma and M. Wei, *J. Am. Chem. Soc.*, 2018, **140**, 11241–11251.
63 Q. Pei, G. Qiu, Y. Yu, J. Wang, K. C. Tan, J. Guo, L. Liu, H. Cao, T. He and P. Chen, *J. Phys. Chem. Lett.*, 2021, **12**, 10646–10653.
64 A. Sarkar, D. Seth, M. Jiang, F. T. T. Ng and G. L. Rempel, *Top. Catal.*, 2014, **57**, 730–740.
65 M. Breysse, E. Furimsky, S. Kasztelan, M. Lacroix and G. Perot, *Catal. Rev.: Sci. Eng.*, 2002, **44**, 651–735.
66 C. H. Hendon, S. T. Hunt, M. Milina, K. T. Butler, A. Walsh and Y. Román-Leshkov, *J. Phys. Chem. Lett.*, 2016, **7**, 4475–4482.
67 D. Mondal, G. Villemure, G. Li, C. Song, J. Zhang, R. Hui, J. Chen and C. Fairbridge, *Appl. Catal., A*, 2013, **450**, 230–236.
68 G. Kresse and J. Furthmüller, *Phys. Rev. B: Condens. Matter Mater. Phys.*, 1996, **54**, 11169–11186.
69 G. Kresse and J. Furthmüller, *Comput. Mater. Sci.*, 1996, **6**, 15–50.
70 J. P. Perdew, K. Burke and M. Ernzerhof, *Phys. Rev. Lett.*, 1996, **77**, 3865–3868.
71 P. E. Blöchl, *Phys. Rev. B: Condens. Matter Mater. Phys.*, 1994, **50**, 17953–17979.
72 G. Kresse and D. Joubert, *Phys. Rev. B: Condens. Matter Mater. Phys.*, 1999, **59**, 1758–1775.